arXiv:2310.08528v1 [cs.CV] 12 Oct 2023

4D Gaussian Splatting for Real-Time Dynamic Scene Rendering

Guanjun Wu[1]*, Taoran Yi[2]*, Jiemin Fang[3], Lingxi Xie[3], Xiaopeng Zhang[3], Wei Wei[1], Wenyu Liu[2], Qi Tian[3], Xinggang Wang[2]†
[1]School of CS, Huazhong University of Science and Technology
[2]School of EIC, Huazhong University of Science and Technology [3]Huawei Inc.
{guajuwu, taoranyi, weiw, liuwy, xgwang}@hust.edu.cn
{jaminfong, 198808xc, zxphistory}@gmail.com tian.qi1@huawei.com

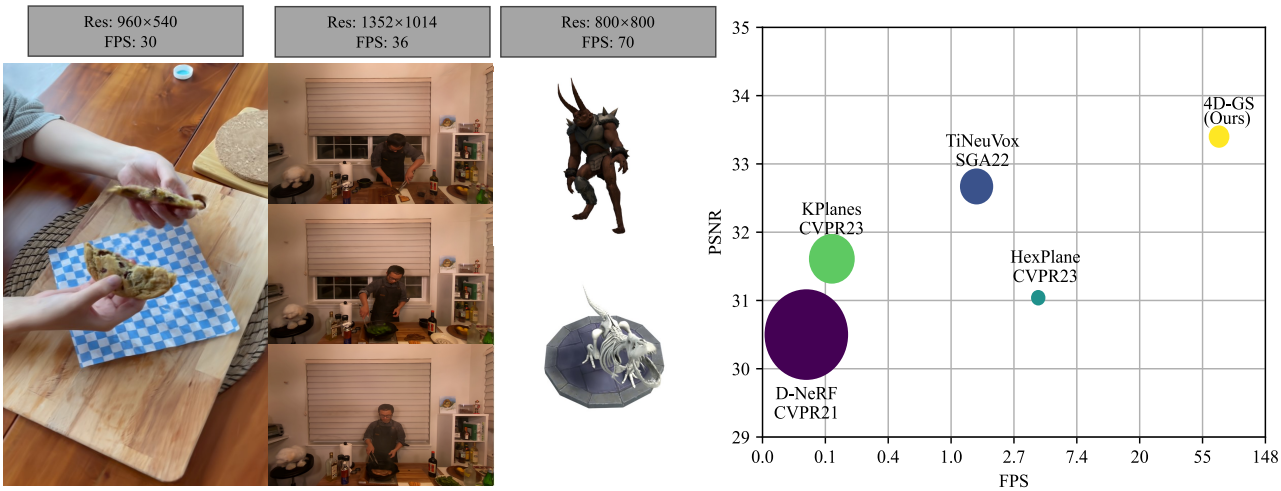

Figure 1. Our method achieves real-time rendering‡ for dynamic scenes at high image resolutions while maintaining high rendering quality. The right figure is mainly tested on synthetic datasets, where the radius of the dot corresponds to the training time. "Res": resolution.

‡The rendering speed not only depends on the rendering resolution, but also the number of 3D Gaussians and the scale of deformation fields which are determined by the complexity of the scene.

Abstract

Representing and rendering dynamic scenes has been an important but challenging task. Especially, to accurately model complex motions, high efficiency is usually hard to maintain. We introduce the 4D Gaussian Splatting (4D-GS) to achieve real-time dynamic scene rendering while also enjoying high training and storage efficiency. An efficient deformation field is constructed to model both Gaussian motions and shape deformations. Different adjacent Gaussians are connected via a HexPlane to produce more accurate position and shape deformations. Our 4D-GS method achieves real-time rendering under high resolutions, 70 FPS at a 800×800 resolution on an RTX 3090 GPU, while maintaining comparable or higher quality than previous state-of-the-art methods. More demos and code are available at https://guanjunwu.github.io/4dgs/.

1. Introduction

Novel view synthesis (NVS) stands as a critical task in the domain of 3D vision and plays a vital role in many applications, *e.g*. VR, AR, movie production *etc*. NVS aims at rendering images from any desired viewpoint or timestamp of a scene, usually requiring to model the scene accurately from several 2D images. Dynamic scenes are quite common in real scenarios, rendering which is important but challenging as complex motions need to be modeled with both spatially and temporally sparse input.

NeRF [20] has achieved great success in synthesizing novel view images by representing scenes with implicit functions. The volume rendering techniques [5] are introduced to connect 2D images and 3D scenes. However, the original NeRF method bears big training and rendering

*Equal contributions.
†Corresponding author.

costs. Though some NeRF variants [3, 6, 7, 9, 21, 32, 34] reduce the training time from days to minutes, the rendering process still bears a non-negligible latency.

Recent 3D Gaussian Splatting (3D-GS) [13] significantly boosts the rendering speed to a real-time level by representing the scene as 3D Gaussians. The cumbersome volume rendering in the original NeRF is replaced with efficient differentiable splatting, which directly projects 3D Gaussian points onto the 2D plane. 3D-GS not only enjoys real-time rendering speed but also represents the scene more explicitly, making it easier to manipulate the scene representation.

However, 3D-GS still focuses on the static scenes. Extending it to dynamic scenes as a 4D representation is a reasonable, important but difficult topic. The key challenge lies in modeling complicated point motions from sparse input. 3D-GS holds a natural geometry prior by representing scenes with point-like Gaussians. One direct and effective extension approach is to construct 3D Gaussians at each timestamp [1, 19] but the storage/memory cost will multiply especially for long input sequences. Our goal is to construct a compact representation while maintaining both training and rendering efficiency, *i.e*. 4D Gaussian Splatting (**4D-GS**). To this end, we

propose to represent Gaussian motions and shape changes by an efficient deformation field, containing a multi-resolution HexPlane and an extremely tiny MLP. Only one set of canonical 3D Gaussians is maintained. For each timestamp, the canonical 3D Gaussians will be transformed by the deformation field into a new position with a new shape. The transformation process represents both the Gaussian motion and deformation. Note that different from modeling motions of each Gaussian separately, the HexPlane can connect different adjacent Gaussians to predict more accurate motions and shape deformation. Then the deformed 3D Gaussians can be directly splatted for rendering the according-timestamp image.

Our contributions can be summarized as follows.

- We introduce an efficient 4D Gaussian Splatting representation by modeling both Gaussian motions and shape changes with a light deformation field.
- The proposed deformation field can connect different adjacent Gaussians with a HexPlane to predict more accurate motions and shape deformations.
- The 4D-GS framework achieves real-time rendering on dynamic scenes, up to 70 FPS at a resolution of 800×800 for synthetic datasets and 36 FPS at a resolution of 1352×1014 in real datasets, while maintaining comparable or superior performance than previous state-of-the-art (SOTA) methods.

2. Related Works

Dynamic Neural Rendering. [2, 20, 45] demonstrate that implicit radiance fields can effectively learn scene representations and synthesize high-quality novel views. Meanwhile, [22, 23, 26] have challenged the static hypothesis, expanding the boundary of novel view synthesis for dynamic scenes. Additionally, [6] proposes to use an explicit voxel grid to model temporal information, accelerating the learning time for dynamic scenes to half an hour. [3, 8, 31] represent further advancements in faster dynamic scene learning. They all utilize a multi-resolution voxel plane model to capture 4D features, leading to high-quality dynamic novel view synthesis and rapid convergence speeds. Additionally, other notable works, namely [4, 14, 38, 41], have put forth effective methodologies for acquiring precise dynamic human body motion information, building upon the foundation provided by the SMPL [18] model. The aforementioned methods though achieve fast training speed, real-time rendering for dynamic scenes is still challenging, especially for monocular input. Our method aims at constructing a highly efficient training and rendering pipeline, while maintaining the quality, even for sparse inputs.

Accelerating Neural Rendering. [12, 29, 43] use pure explicit representations or the baking method to promote the rendering speed but mainly focus on the static scenes. Some works [25, 36] aim at accelerating the rendering on dynamic scenes but dense input images or additional geometry priors are required. It becomes a growing demand to achieve general real-time rendering methods for dynamic scenes. 3D Gaussian splatting (3D-GS) [13], an effective scene representation and rendering method, has been developed that not only achieves fast convergence speeds but is also easily integrated into the graphics rendering pipeline, making real-time rendering of general scenes more accessible. Our method extends 3D-GS [13] to 4D, named 4D-GS, achieving real-time rendering for general dynamic scenes that can be applied easily with both monocular and multi-view input.

Neural Rendering with Point Clouds. Effectively representing 3D scenes remains a challenging topic. The community has explored various neural representations [20], *e.g*. meshes, point clouds [39], and hybrid approaches. Point-cloud-based methods [16, 27, 28, 44] initially target at 3D segmentation and classification. A representative approach for rendering presented in [39] combines point cloud representations with volume rendering, achieving rapid convergence. However, implicit features in point clouds limited rendering speed. [1] uses an explicit point cloud approach with velocity vectors for online training. Additionally, 3D-GS [13] is notable for its pure explicit representation and differential point-based splatting methods, enabling real-time rendering of novel views. Recently, Dynamic3DGS [19] has incorporated 3D-GS into tasks related

to dynamic scene novel-view synthesis. Dynamic3DGS models dynamic scenes by tracking the position and variance of each Gaussian at each timestamp t_i. This method effectively captures dynamic scenes when dense multi-view inputs are available, but it encounters difficulties in accurately modeling monocular dynamic scenes. Specifically, Dynamic3DGS relies on modeling results from the previous timestamp t_{i-1}. With dense multi-view inputs, the modeling results from the previous timestamp are accurate, allowing for effective modeling at the current timestamp based on these results. Additionally, an explicit table is utilized to store information about each 3D Gaussian at every timestamp, leading to a linear memory consumption increase, denoted as $O(tN)$, in which N is num of 3D Gaussians. For long-term scene reconstruction, the storage cost will become non-negligible. The memory complexity of our approach only depends on the number of 3D Gaussians and parameters of Gaussians deformation fields $\mathcal{V}$, which is denoted as $O(N + \mathcal{V})$. Meanwhile, Deformable 3DGS [40] is a recurrent work that introduces an MLP deformation network to model the motion of dynamic scenes. Our approach also models Gaussian motions but with a compact field, resulting in highly efficient training efficiency and real-time rendering.

3. Preliminary

In this section, we simply review the representation and rendering process of 3D-GS [13] in Sec. 3.1 and the formula of dynamic NeRFs based on deformation fields in Sec. 3.2.

3.1. 3D Gaussian Splatting

3D-GS [13] is an explicit 3D scene representation in the form of point clouds, utilizing Gaussians to model the scene. Each Gaussian is characterized by a covariance matrix Σ and a center point $\mathcal{X}$, which is referred to as the mean value of the Gaussian:

$$G(X) = e^{-\frac{1}{2}\mathcal{X}^T \Sigma^{-1} \mathcal{X}}. \tag{1}$$

For differentiable optimization, the covariance matrix Σ can be decomposed into a scaling matrix $\mathbf{S}$ and a rotation matrix $\mathbf{R}$:

$$\Sigma = \mathbf{RSS}^T\mathbf{R}^T, \tag{2}$$

the computation of gradient flow during training is depicted in [13].

When rendering novel views, the technique of splatting [42] is employed for the Gaussians within the camera planes. As introduced by [47], using a viewing transform denoted as W and the Jacobian of the affine approximation of the projective transformation represented by J, the covariance matrix Σ' in camera coordinates can be computed as follows:

$$\Sigma' = JW\Sigma W^T J^T. \tag{3}$$

In summary, each Gaussian point is characterized by the following attributes: position $\mathcal{X} \in \mathbb{R}^3$, color defined by spherical harmonics coefficients $\mathcal{C} \in \mathbb{R}^k$ (where k represents the degrees of freedom), opacity $\alpha \in \mathbb{R}$, rotation factor $r \in \mathbb{R}^4$, and scaling factor $s \in \mathbb{R}^3$. Specifically, for each pixel, the color and opacity of all the Gaussians are computed using the Gaussian's representation Eq. 1. The blending of N ordered points that overlap the pixel is given by the formula:

$$C = \sum_{i \in N} c_i \alpha_i \prod_{j=1}^{i-1} (1 - \alpha_i). \tag{4}$$

Here, c_i, α_i represents the density and color of this point computed by a Gaussian with covariance Σ multiplied by an optimizable per-point opacity and SH color coefficients.

3.2. Dynamic NeRFs with Deformation Fields

Dynamic NeRFs mainly follow two paths: canonical-mapping volume rendering [6, 17, 22, 23, 26] and directly modeling [3, 9, 10]. To sum up, All the algorithms can be written as the following equation:

$$c, \sigma = \mathbb{G}(\mathbf{x}, t), \tag{5}$$

where $\mathbb{G}$ is a neural representation of the scene. Given any position $\mathbf{x} = \{x, y, z\}$ and timestamp t, a neural module is employed to compute color C and density σ. Then, the discrete volume rendering equation Eq. 4 [5] is applied to integrate spatial color and density into pixel color.

Meanwhile, the canonical-mapping volume rendering mapping each sampled point into another canonical space at a given timestamp t, and the other treats timestamp t as a feature same with position $\mathbf{x}$ and view direction d. Using a deformation field is a straightforward process because the tracing of the casted rays is Interpretable. Given a sampled point $\mathbf{x} = \{x, y, z\}$, a deformation fields $\mathcal{F}$ is adopted to compute its deformed position $\mathbf{x}'$:

$$\mathbf{x}' = \mathcal{F}(\mathbf{x}, \mathbf{t}). \tag{6}$$

Then, any NeRF-based methods can be applied in the deformed point $\mathbf{x}$ to calculate the final color and density.

$$c, \sigma = \mathbb{G}'(x'). \tag{7}$$

In most cases [6, 10, 23, 23, 26], positional encoding [35] is used to expand information.

4. Methods

This section introduces our 4D Gaussian Splatting framework in Sec. 4.1. Then, an efficient voxel-based deformation field is discussed in Sec. 4.2. Finally, we display the optimization process in Sec. 4.3.

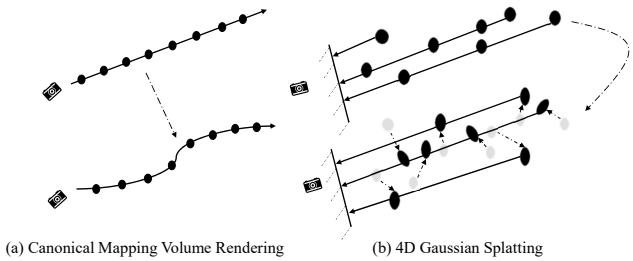

Figure 2. Illustration of canonical mapping volume rendering and 4D Gaussian Splatting.(a) Points are sampled ray during volume rendering. Arrows stand for the casted rays, linear arrows are transformed into curve after canonical mapping.(b) Points stand for 3D Gaussians. Arrows stand for the splatting process among each pixel.

4.1. 4D Gaussian Splatting

Adopting a deformation field to encode 4D information is a common approach in related works [6, 26]. Given a rendered pixel, a ray r is cast. The sampled points x and timestamp t are fed into an MLP to map into a canonical space and applied with volume rendering [5]. However, each point on the sample ray may own different velocity variables, which causes heavily different deformation, as shown in Fig. 2, after applying canonical mapping, the position of each ray is changed. so the volume rendering process may become inaccurate. Meanwhile, differential splatting [42] creates a relationship among 3D Gaussians on the rendered pixel directly, therefore, each rendered pixel may influenced by different 3D Gaussians every timestamp. The differential splatting is still meaningful. Therefore, we only maintain one set of canonical 3D Gaussians, what we need to do is to employ deformation fields $\mathcal{F}$ to predict each 3D Gaussian's state at a given timestamp t. Given a view-matrix $[R, T]$, the differential splatting [42] Eq. 4 (written as $\mathcal{G}$) is adopted to render a pixel color.

$$\hat{C} = \mathcal{G}(\mathcal{S}'|R, T). \tag{8}$$

The goal of our task is to learn proper 3D Gaussians $\mathcal{S}$ and deformation module $\mathcal{F}$, then we can compute the 3D Gaussians' information $\mathcal{S}' = [\mathcal{X}'^{*}, s', r', \sigma, \mathcal{C}]$ at time t:

$$\mathcal{S}' = \mathcal{F}(\mathcal{S}, t), \tag{9}$$

Where $\mathcal{F}$ is our proposed Gaussians deformation fields, which will be discussed in Sec. 4.2. σ is the opacity of each 3D Gaussian and $\mathcal{C}$ stands for SH coefficient which can model the color of each 3D Gaussian c.

The quest for an efficient method that can capture nearby 3D Gaussian information while maintaining both high rendering quality and fast rendering speed is of paramount importance. As depicted in Fig. 3, we employ multi-resolution neural voxels to establish relationships between 3D Gaussians. This approach encodes deformations within the unit voxel grid using only four neighboring points, thus significantly reducing memory consumption. Subsequently, we introduce a compact MLP, which in conjunction with the multi-resolution neural voxels, efficiently merges deformation features and ensures rapid forward-pass speed during rendering. Finally, all features are decoded by separate MLP.

*Deformed 3D Gaussian's position: $\mathcal{X}' = \{x', y', z'\}$

4.2. Gaussian Deformation Fields

Our Gaussian deformation field $\mathcal{F}$ can be decomposed into two modules, *i.e.* multi-resolution neural voxels and decoder MLP g. The formula of multi-resolution neural voxels will be introduced in the following paragraph and the decoder will be discussed after that.

3D Gaussian Neural Voxel Encoding. As illustrated in Fig. 4, nearby 3D Gaussians always share similar deformation(motion and shape changes) while the same 3D Gaussians also own similar features between nearby timestamps. Besides, the relationship between far-distant 3D Gaussians cannot be ignored. There should be a proper structure to encode all the 3D Gaussians' information within unit voxels. As a result, we adopt a multi-resolution HexPlane voxel module to encode the spatial and temporal information of each 3D Gaussian. Each voxel module is defined by $R(i, j) \in \mathbb{R}^{h \times lN_i \times lN_j}$, where h stand for hidden dim of features, lN denoted as the resolution of each dim and l equal to upsampling scales. This entails encoding information of the 3D Gaussians within six 2D voxel planes while considering temporal information. The formula for computing separate voxel features is as follows :

$$f_{voxel} = \bigcup_{l} \prod P(i, j), \text{where } P(i, j) = \text{interp}(R(i, j)),$$
$$\{i, j\} \in \{(x, y), (x, z), (y, z), (x, t), (y, t), (z, t)\}. \tag{10}$$

The voxel feature $f_{voxel_i} \in \mathbb{R}^{h*l}$ is the hidden feature of neural voxels. and we utilize bilinear interpolation to interpolate the four nearby queried voxel features.

In the compact representation of 3D Gaussians, the position $\mathcal{X}$ and time t of these 3D Gaussians play a crucial role in encoding their motion. Besides, as shown in Fig. 5, during the optimization, the point of Gaussians are become denser, which means that the covariance of 3D Gaussians is decreasing. Meanwhile, when we introduce additional parameters like covariance values s and r into these 3D Gaussians, it increases the computational demands, which in turn leads to a slowdown in both rendering and training speeds. So we conclude that the covariance of Gaussians will become less important during the optimization. Therefore, we decide to omit the 3D Gaussian's rotation and scaling

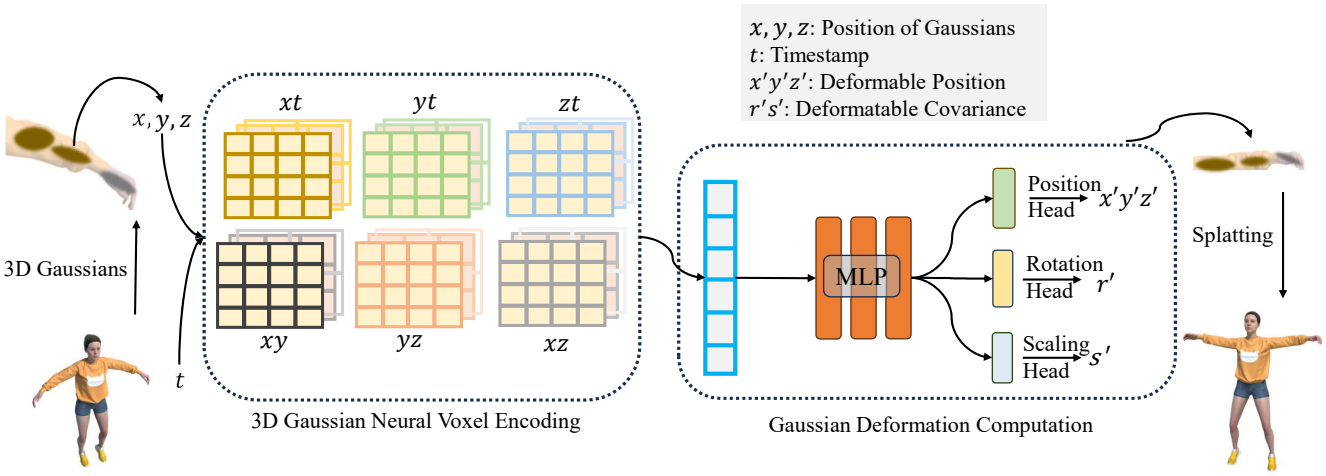

Figure 3. The overall pipeline of our model. Given a group of 3D Gaussians $\mathcal{S}$, we extract the center coordinate of each 3D Gaussian $\mathcal{X}$ and timestamp t to compute the voxel feature by querying multi-resolution voxel planes. Then a tiny MLP is used to decode the feature and get $\mathcal{S}'$ of each Gaussian at timestamp t. The deformed Gaussians are then splatted to render the image.

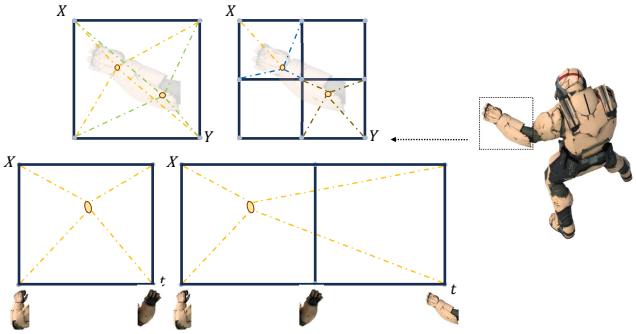

Figure 4. Illustration of querying multi-resolution voxel grids.

information and focus solely on the position $\mathcal{X}$ and given timestamp t.

Gaussians Deformation Computation. When the all information of 3D Gaussians is encoded, we can compute any desired variable with a tiny encoder. Therefore, a compact decoder layer g proves to be sufficient for decoding and merging all the necessary information. Finally, separate MLP regressors are employed to compute the deformation of position $\Delta\mathcal{X}$, rotation Δr, and scaling Δs.

$$\Delta\mathcal{X}, \Delta r, \Delta s = g(f_{voxel}). \tag{11}$$

Then, the deformed feature $(\mathcal{X}', r', s')$ can be computed as:

$$(\mathcal{X}', r', s') = (\mathcal{X} + \Delta\mathcal{X}, r + \Delta r, s + \Delta s). \tag{12}$$

Finally, we obtain the deformed 3D Gaussians $S' = \{\mathcal{X}', s', r', \sigma, \mathcal{C}\}$.

4.3. Optimization

Static 3D Gaussians Initialization. In the context of dynamic scene reconstruction, both camera motion and object motion can introduce challenges in representation learning. To address this, several methods such as [11, 17] employ separate branches to recover the static and dynamic parts of the scene independently. Notably, [13] has highlighted that the quality of reconstruction is influenced, in part, by the initialization of 3D Gaussians. Additionally, random initialization of deformation fields can impact training convergence.

To mitigate these issues, we have adopted two training strategies. In the initial stage, known as the *static stage*, we focus on finding an appropriate initialization for the scene, optimizing only the parameters of 3D Gaussians. The fine-tuning stage then follows, where we learn the deformation fields. We illustrate the training process in Fig. 5.

Loss Function. Similar to other reconstruction methods [6, 13, 26], we also use the reconstruction loss to supervise the training process, and grid-based TV Loss [3, 6, 9, 34]$\mathcal{L}_{tv}$ is also added into our loss functions.

$$\mathcal{L} = (\hat{C} - C)^2 + \mathcal{L}_{tv}. \tag{13}$$

5. Experiments

In this section, we mainly introduce the hyperparameters and datasets of our settings in Sec 5.1. Then, the results between different datasets will be compared with [3, 6, 9, 13, 33] in Sec. 5.2. Finally, ablation studies are proposed to prove the effectiveness of our approaches in Sec. 5.3.

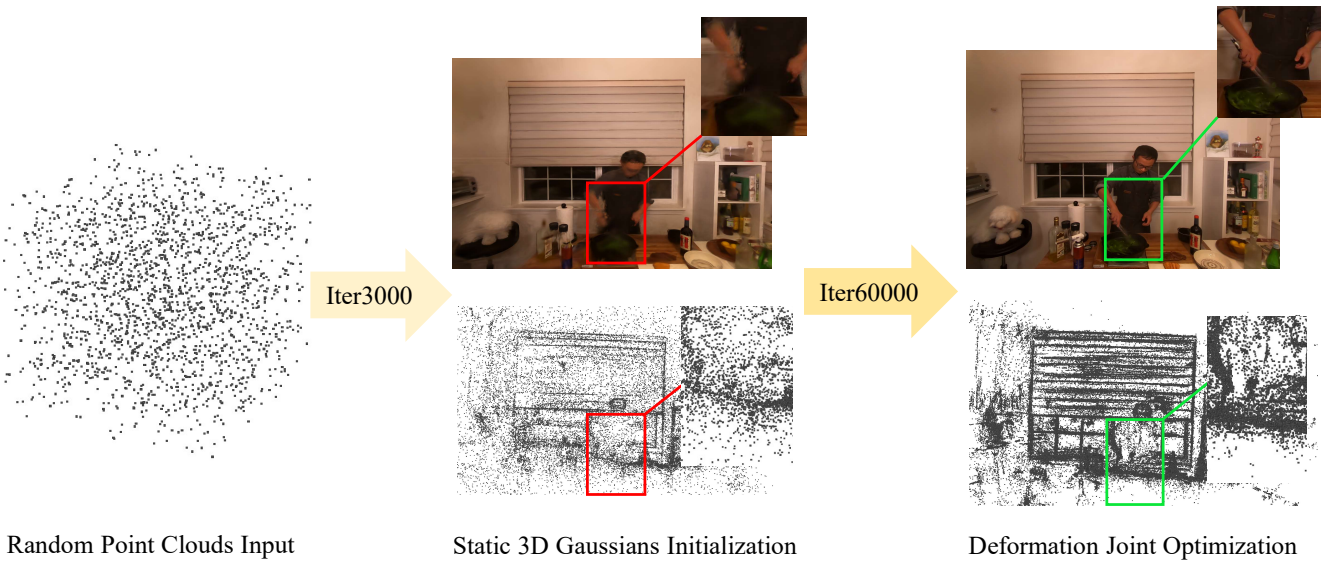

Figure 5. Illustration of the optimization process. With static 3D Gaussian initialization, our model can learn high-quality 3D Gaussians of the motion part. Meanwhile, without sfm [30] points initialized, the scene's point cloud becomes dense.

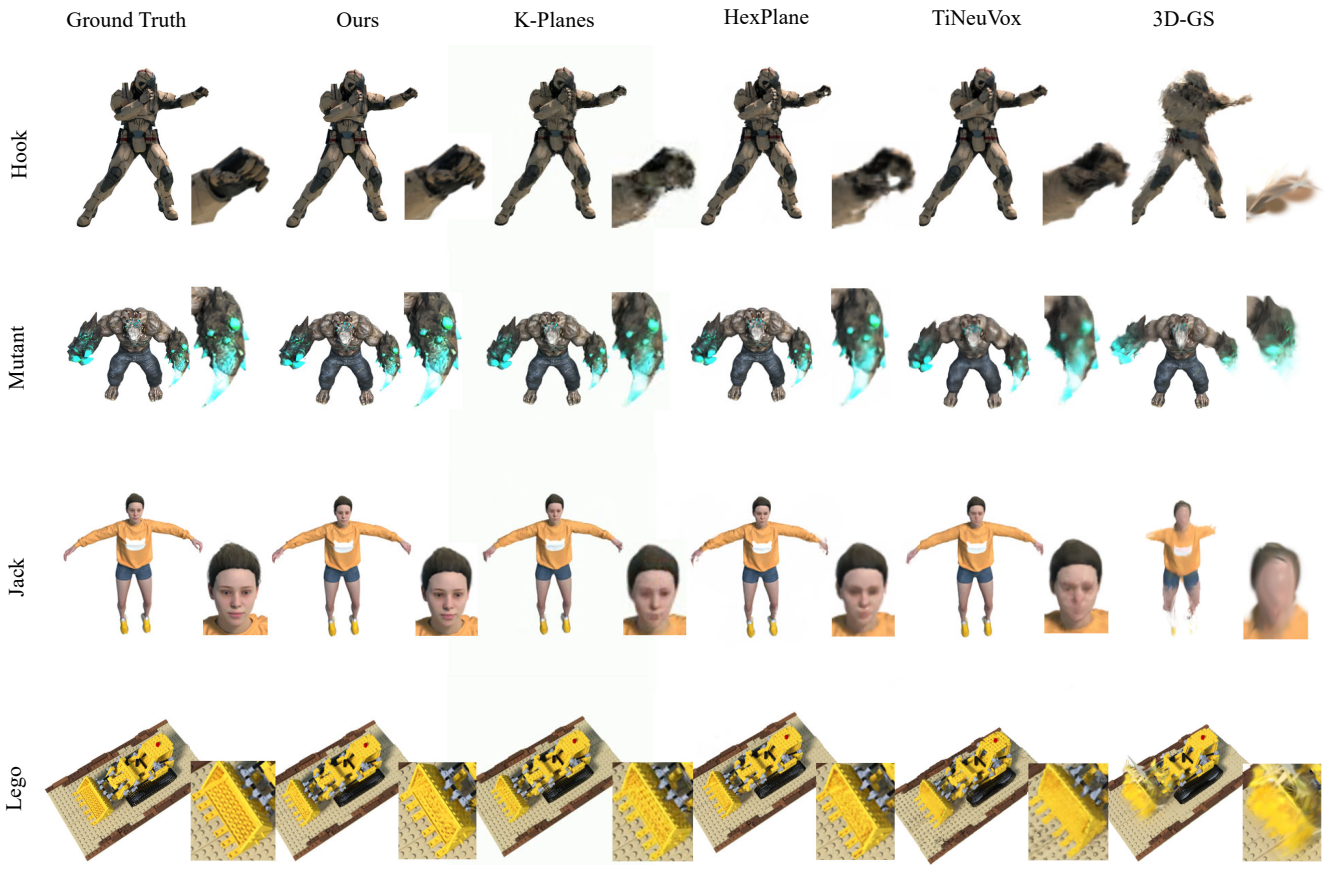

Figure 6. Visualization of synthesized datasets compared with the model. The rendering results of [9] are displayed with a default green background. We have adopted their rendering settings.

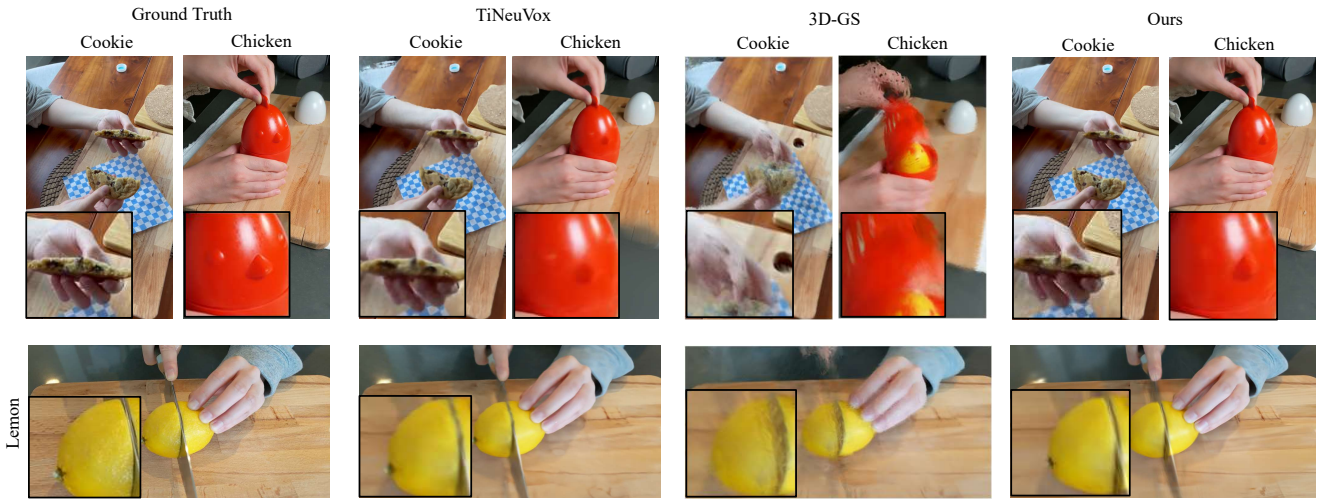

Figure 7. Visualization of the HyperNeRF[23] datasets compared with our model.

Table 1. Quantitative results on synthesis dataset. The rendering resolution is set to 800×800. "Time" in the table stands for training times.

Model	PSNR(dB)↑	SSIM↑	LPIPS↓	Time↓	FPS ↑	Storage (MB) ↓	FPS/Stoarge(FPS/MB)↑
TiNeuVox-B [6]	32.67	0.97	0.04	28 mins	∼ 1.5	48	0.03125
KPlanes [9]	31.61	0.97	/	52 mins	∼ 0.12	∼ 470	0.000255
HexPlane-Slim [3]	31.04	0.97	0.04	11m 30s	4	∼ 70	0.057
3D-GS [13]	15.76	0.69	0.07	**10 mins**	**170**	**∼10**	**21.25**
4D-GS (Ours)	**33.30**	**0.98**	**0.03**	20 mins	70	∼ 163	0.438

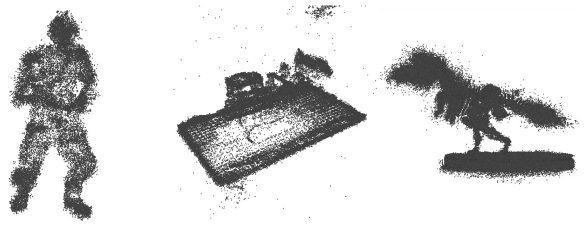

Figure 8. Visualization of dynamic scene point clouds.

5.1. Experimental Settings

Our implementation is primarily based on the PyTorch [24] framework, and we've fine-tuned our optimization parameters by the configuration outlined in the 3dgs [13] paper. Notably, we have configured the intervals for point cloud pruning to be set at 8000, and the total training iterations decrease to 20000. Additionally, we have established the voxel plane resolution as $[64, 64]$, integrating multi-resolution upsampling at levels $L = \{2, 4, 8\}$. Following a similar approach to that elucidated in [8], each plane is endowed with hidden features set to a dimension of 32.

Moreover, the default setting for the hidden layer of the MLP decoder is 64, and the learning rate is initially set at 1.6e-4, gradually decreasing exponentially to 1.6e-6 by the end of the training process. The learning rate for the voxel grid is initialized at 1.6e-3 and exponentially decays to 1.6e-5. All the experiments are tested in a single RTX 3090 GPU.

Synthetic Dataset. We primarily assess the performance of our model using synthetic datasets, as introduced by D-NeRF [26]. These datasets are designed for monocular settings, although it's worth noting that the camera poses for each timestamp are close to randomly generated. Each scene within these datasets contains dynamic frames, ranging from 50 to 200 in number.

Real-world Datasets. We utilize datasets provided by Nerfies [23] and DyNeRF's [15] as benchmark datasets to evaluate the performance of our model in real-world scenarios. The Nerfies dataset is captured using one or two cameras, following straightforward camera motion, while the DyNeRF's dataset is captured using 15 to 20 static cameras, involving extended periods and intricate camera motions.

5.2. Results

We primarily assess our experimental results using various metrics, encompassing PSNR, SSIM [37], LPIPS [46], FPS, and Storage. Furthermore, we delve into the specific aspects

Table 2. Our model evaluation is focused exclusively on scenes featuring *chicken*, *split-cookies*, *cut-lemons*, and *3d-printer*. Rendering resolution is set to 960×540.

Model	PSNR(dB)↑	SSIM↑	LPIPS↓	Times↓	FPS↑	Storage (MB)↓	FPS/Stoarge(FPS/MB)↑
TiNeuVox-B [6]	26.87	0.75	0.37	50 mins	∼ 0.5	48	0.010
3D-GS [13]	20.84	0.70	0.45	**7 mins**	**71**	**36**	**1.972**
4D-GS (Ours)	**26.98**	**0.78**	**0.31**	54 mins	30	184	0.163

Table 3. Quantitative results on the DyNeRF's [15] dataset, specifically for the *Spinach*, *Beef*, and *Steak scenes*. Results from [3, 9, 33] are referenced from their respective papers. Rendering resolution is set to 1386×1014.

Model	PSNR(dB)↑	SSIM↑	LPIPS↓	Times↓	FPS↑	Storage (MB)↓	FPS/Stoarge(fps/MB)↑
HexPlane [3]	**32.22**	**0.98**	**0.09**	12 h	0.21	252	0.00083
KPlanes [9]	31.82	0.97	-	∼4 h	0.15	309	0.00049
NeRFPlayer[33]	32.07	0.93	0.12	5.5h	0.09	-	-
4D-GS (Ours)	31.02	0.94	0.15	**2 h**	**36**	145	0.248

Figure 9. Ablation Study of two stages training. Without static point cloud initialization, Gaussians may go into local minimum and suffer from a worse quality.

of the FPS/Storage ratio. As demonstrated in Tab. 1, our methods consistently achieve state-of-the-art results across a comprehensive range of metrics. Notably, our approach stands out with its relatively swift training pace and exceptionally rapid rendering speed, achieving over 50 FPS at a resolution of 800×800.

To assess the quality of novel view synthesis, we conducted benchmarking against several state-of-the-art methods in the field, including [3, 6, 9, 33]. The results are summarized in Tab. 1. While current dynamic hybrid representations can produce high-quality results, they often come with the drawback of slow training times. The lack of modeling dynamic motion part makes [13] fail to Additionally, rendering speed is typically constrained by volume rendering and multiple neural unit queries. In contrast, our method strikes a balance between convergence speed, rendering quality, and rendering speed. It achieves the highest rendering quality within the synthesis dataset while also delivering exceptionally fast rendering speeds. While 3D-GS [13] demonstrates exceptional speed in terms of convergence and rendering, its limitations become evident in its inability to effectively learn and render the dynamic aspects of the scenes. Consequently, this shortcoming results in a significant reduction in rendering quality.

In addition, the results obtained from real-world datasets are presented in Tab. 2 and Fig. 3. As illustrated in Fig. 7, it becomes apparent that grid-based NeRF methods, such as TiNeuVox [6], encounter difficulties when attempting to capture intricate object details. In stark contrast, our proposed methods exhibit a remarkable ability to preserve these intricate details. Furthermore, visualizations of [15] datasets are also featured in Fig. 10. Notably, our methods not only excel in modeling complex object motions but also excel in rendering high-quality free-view images using multi-view image inputs.

5.3. Ablation Study

Neural Voxel Encoder. The explicit neural voxel encoder possesses the capacity to retain 3D Gaussians' deformation information, striking a balance between pure implicit MLP approaches[40] and purely explicit status table-based methods[19]. Discarding this module, we observe that using only shallow MLPs falls short in modeling complex deformations across various settings. Tab. 4 demonstrates that, while the model incurs minimal memory costs, it does come at the expense of rendering quality.

Model Capacity. Undoubtedly, expanding the model's size, be it through increased voxel plane resolutions or deeper MLP decoders, can significantly elevate rendering quality. However, this enhancement invariably carries the trade-off of diminished rendering speed, owing to the heightened computational demands imposed by larger models. Tab. 4 provides concrete evidence of this trade-off. When we augment the hidden layer of the MLP to a size of 256, we observe a noteworthy improvement in rendering quality, translating to an approximate gain of 0.25 dB.

Table 4. Conducting an Ablation Study on Synthetic Datasets Using Our Proposed Methods. Relocating explicit voxels can expedite training and rendering speed; however, it compromises the ability to generate high-quality images.

Model	PSNR(dB)↑	SSIM↑	LPIPS↓	Time↓	FPS↑	Storage (MB)↓	FPS/Stoarge(fps/MB)↑
Ours w/o Voxel Grid	27.05	0.95	0.05	10 mins	**140**	**15**	**9.333**
Ours w/o Static Stage	31.91	0.97	0.03	19 mins	69	161	0.428
Ours w/ Image Loss	32.74	0.97	0.02	42 mins	51	204	0.250
Ours w/ Larger MLP	**33.55**	**0.98**	0.03	22 mins	66	164	0.402
Ours-7k	30.04	0.97	0.04	**7 mins**	67	162	0.413
Ours	33.30	0.98	**0.03**	20 mins	70	163	0.429

Two Stage Training. In datasets such as D-NeRF [26] and DyNeRF [15], there is no prior point cloud information available for initializing 3D Gaussians. Consequently, training the model to learn both 3D Gaussians and deformation fields becomes considerably more challenging compared to static scenes. To address this issue, we adopt the strategy of optimizing 3D Gaussians exclusively, allowing the model to establish a suitable initialization for learning the motion fields. As illustrated in Fig. 9, through a brief static training stage of just $N = 3000$ iterations (lasting no more than 2 minutes), we observe a notable improvement of approximately 1.5 dB in the PSNR of the scene.

Fast Training. Conversely, stopping the model's training at iteration 7k can still yield relatively good results, this approach has the potential to train a faster coarse model. The results of fast training are also displayed in Tab. 4.

Image-based Loss. We owe a significant portion of our progress to the splatting algorithm. In every training stage, an image is generated by the model based on the provided training camera pose. This allows us to apply LPIPS-based [46] Loss and SSIM-based [37] Loss during the training process. However, it's essential to acknowledge that this inclusion does slow down the training speed by over 2 times, potentially impeding real-time rendering. It may be because optimizing the motion part is a hard and complex process. Adding image-based loss may trigger worse cases. As a result, during the training stage, we have chosen to decelerate this process to ensure more efficient model training.

6. Conclusion

In this paper, we propose 4D Gaussian Splatting to achieve real-time dynamic scene rendering. An efficient deformation field is constructed to accurately model Gaussian motions and shape deformations, where adjacent Gaussians are connected via HexPlane representation. Connections between Gaussians lead to more complete deformed geometry, effectively avoiding avulsion. This work is still in progress and we will explore higher rendering quality on complex real scenes in the subsequent development.

Figure 10. Visualization of DyNeRF's rendering results through our model, as referenced in [15].

References

[1] Jad Abou-Chakra, Feras Dayoub, and Niko Sünderhauf. Particlenerf: Particle based encoding for online neural radiance fields in dynamic scenes. *arXiv preprint arXiv:2211.04041*, 2022. 2

[2] Jonathan T Barron, Ben Mildenhall, Matthew Tancik, Peter Hedman, Ricardo Martin-Brualla, and Pratul P Srinivasan. Mip-nerf: A multiscale representation for anti-aliasing neural radiance fields. In *Proceedings of the IEEE/CVF International Conference on Computer Vision*, pages 5855–5864, 2021. 2

[3] Ang Cao and Justin Johnson. Hexplane: A fast representation for dynamic scenes. In *Proceedings of the IEEE/CVF Conference on Computer Vision and Pattern Recognition*, pages 130–141, 2023. 2, 3, 5, 7, 8

[4] Zhaoxi Chen and Ziwei Liu. Relighting4d: Neural relightable human from videos. In *European Conference on Computer Vision*, pages 606–623. Springer, 2022. 2

[5] Robert A Drebin, Loren Carpenter, and Pat Hanrahan. Volume rendering. *ACM Siggraph Computer Graphics*, 22(4): 65–74, 1988. 1, 3, 4

[6] Jiemin Fang, Taoran Yi, Xinggang Wang, Lingxi Xie, Xiaopeng Zhang, Wenyu Liu, Matthias Nießner, and Qi Tian. Fast dynamic radiance fields with time-aware neural vox-

els. In *SIGGRAPH Asia 2022 Conference Papers*, pages 1–9, 2022. 2, 3, 4, 5, 7, 8

[7] Sara Fridovich-Keil, Alex Yu, Matthew Tancik, Qinhong Chen, Benjamin Recht, and Angjoo Kanazawa. Plenoxels: Radiance fields without neural networks. In *Proceedings of the IEEE/CVF Conference on Computer Vision and Pattern Recognition*, pages 5501–5510, 2022. 2

[8] Sara Fridovich-Keil, Giacomo Meanti, Frederik Rahbæk Warburg, Benjamin Recht, and Angjoo Kanazawa. K-planes: Explicit radiance fields in space, time, and appearance. In *Proceedings of the IEEE/CVF Conference on Computer Vision and Pattern Recognition*, pages 12479–12488, 2023. 2, 7

[9] Sara Fridovich-Keil, Giacomo Meanti, Frederik Rahbæk Warburg, Benjamin Recht, and Angjoo Kanazawa. K-planes: Explicit radiance fields in space, time, and appearance. In *Proceedings of the IEEE/CVF Conference on Computer Vision and Pattern Recognition*, pages 12479–12488, 2023. 2, 3, 5, 6, 7, 8

[10] Chen Gao, Ayush Saraf, Johannes Kopf, and Jia-Bin Huang. Dynamic view synthesis from dynamic monocular video. In *Proceedings of the IEEE/CVF International Conference on Computer Vision*, pages 5712–5721, 2021. 3

[11] Chen Gao, Ayush Saraf, Johannes Kopf, and Jia-Bin Huang. Dynamic view synthesis from dynamic monocular video. In *Proceedings of the IEEE/CVF International Conference on Computer Vision*, pages 5712–5721, 2021. 5

[12] Peter Hedman, Pratul P Srinivasan, Ben Mildenhall, Jonathan T Barron, and Paul Debevec. Baking neural radiance fields for real-time view synthesis. In *Proceedings of the IEEE/CVF International Conference on Computer Vision*, pages 5875–5884, 2021. 2

[13] Bernhard Kerbl, Georgios Kopanas, Thomas Leimkühler, and George Drettakis. 3d gaussian splatting for real-time radiance field rendering. *ACM Transactions on Graphics (ToG)*, 42(4):1–14, 2023. 2, 3, 5, 7, 8

[14] Chen Li, Jihao Lin, and Gim Hee Lee. Ghunerf: Generalizable human nerf from a monocular video. *arXiv preprint arXiv:2308.16576*, 2023. 2

[15] Tianye Li, Mira Slavcheva, Michael Zollhoefer, Simon Green, Christoph Lassner, Changil Kim, Tanner Schmidt, Steven Lovegrove, Michael Goesele, Richard Newcombe, et al. Neural 3d video synthesis from multi-view video. In *Proceedings of the IEEE/CVF Conference on Computer Vision and Pattern Recognition*, pages 5521–5531, 2022. 7, 8, 9

[16] Xingyu Liu, Mengyuan Yan, and Jeannette Bohg. Meteornet: Deep learning on dynamic 3d point cloud sequences. In *Proceedings of the IEEE/CVF International Conference on Computer Vision*, pages 9246–9255, 2019. 2

[17] Yu-Lun Liu, Chen Gao, Andreas Meuleman, Hung-Yu Tseng, Ayush Saraf, Changil Kim, Yung-Yu Chuang, Johannes Kopf, and Jia-Bin Huang. Robust dynamic radiance fields. In *Proceedings of the IEEE/CVF Conference on Computer Vision and Pattern Recognition*, pages 13–23, 2023. 3, 5

[18] Matthew Loper, Naureen Mahmood, Javier Romero, Gerard Pons-Moll, and Michael J Black. Smpl: A skinned multi-person linear model. In *Seminal Graphics Papers: Pushing the Boundaries, Volume 2*, pages 851–866. 2023. 2

[19] Jonathon Luiten, Georgios Kopanas, Bastian Leibe, and Deva Ramanan. Dynamic 3d gaussians: Tracking by persistent dynamic view synthesis. *preprint*, 2023. 2, 8

[20] Ben Mildenhall, Pratul P Srinivasan, Matthew Tancik, Jonathan T Barron, Ravi Ramamoorthi, and Ren Ng. Nerf: Representing scenes as neural radiance fields for view synthesis. *Communications of the ACM*, 65(1):99–106, 2021. 1, 2

[21] Thomas Müller, Alex Evans, Christoph Schied, and Alexander Keller. Instant neural graphics primitives with a multiresolution hash encoding. *ACM Transactions on Graphics (ToG)*, 41(4):1–15, 2022. 2

[22] Keunhong Park, Utkarsh Sinha, Jonathan T Barron, Sofien Bouaziz, Dan B Goldman, Steven M Seitz, and Ricardo Martin-Brualla. Nerfies: Deformable neural radiance fields. In *Proceedings of the IEEE/CVF International Conference on Computer Vision*, pages 5865–5874, 2021. 2, 3

[23] Keunhong Park, Utkarsh Sinha, Peter Hedman, Jonathan T Barron, Sofien Bouaziz, Dan B Goldman, Ricardo Martin-Brualla, and Steven M Seitz. Hypernerf: A higher-dimensional representation for topologically varying neural radiance fields. *arXiv preprint arXiv:2106.13228*, 2021. 2, 3, 7

[24] Adam Paszke, Sam Gross, Francisco Massa, Adam Lerer, James Bradbury, Gregory Chanan, Trevor Killeen, Zeming Lin, Natalia Gimelshein, Luca Antiga, et al. Pytorch: An imperative style, high-performance deep learning library. *Advances in neural information processing systems*, 32, 2019. 7

[25] Sida Peng, Yunzhi Yan, Qing Shuai, Hujun Bao, and Xiaowei Zhou. Representing volumetric videos as dynamic mlp maps. In *Proceedings of the IEEE/CVF Conference on Computer Vision and Pattern Recognition*, pages 4252–4262, 2023. 2

[26] Albert Pumarola, Enric Corona, Gerard Pons-Moll, and Francesc Moreno-Noguer. D-nerf: Neural radiance fields for dynamic scenes. In *Proceedings of the IEEE/CVF Conference on Computer Vision and Pattern Recognition*, pages 10318–10327, 2021. 2, 3, 4, 5, 7, 9

[27] Charles R Qi, Hao Su, Kaichun Mo, and Leonidas J Guibas. Pointnet: Deep learning on point sets for 3d classification and segmentation. In *Proceedings of the IEEE conference on computer vision and pattern recognition*, pages 652–660, 2017. 2

[28] Charles Ruizhongtai Qi, Li Yi, Hao Su, and Leonidas J Guibas. Pointnet++: Deep hierarchical feature learning on point sets in a metric space. *Advances in neural information processing systems*, 30, 2017. 2

[29] Christian Reiser, Songyou Peng, Yiyi Liao, and Andreas Geiger. Kilonerf: Speeding up neural radiance fields with thousands of tiny mlps. In *Proceedings of the IEEE/CVF International Conference on Computer Vision*, pages 14335–14345, 2021. 2

[30] Johannes L Schonberger and Jan-Michael Frahm. Structure-from-motion revisited. In *Proceedings of the IEEE con-*

ference on computer vision and pattern recognition, pages 4104–4113, 2016. 6

[31] Ruizhi Shao, Zerong Zheng, Hanzhang Tu, Boning Liu, Hongwen Zhang, and Yebin Liu. Tensor4d: Efficient neural 4d decomposition for high-fidelity dynamic reconstruction and rendering. In *Proceedings of the IEEE/CVF Conference on Computer Vision and Pattern Recognition*, pages 16632–16642, 2023. 2

[32] Ruizhi Shao, Zerong Zheng, Hanzhang Tu, Boning Liu, Hongwen Zhang, and Yebin Liu. Tensor4d: Efficient neural 4d decomposition for high-fidelity dynamic reconstruction and rendering. In *Proceedings of the IEEE/CVF Conference on Computer Vision and Pattern Recognition*, pages 16632–16642, 2023. 2

[33] Liangchen Song, Anpei Chen, Zhong Li, Zhang Chen, Lele Chen, Junsong Yuan, Yi Xu, and Andreas Geiger. Nerfplayer: A streamable dynamic scene representation with decomposed neural radiance fields. *IEEE Transactions on Visualization and Computer Graphics*, 29(5):2732–2742, 2023. 5, 8

[34] Cheng Sun, Min Sun, and Hwann-Tzong Chen. Direct voxel grid optimization: Super-fast convergence for radiance fields reconstruction. In *Proceedings of the IEEE/CVF Conference on Computer Vision and Pattern Recognition*, pages 5459–5469, 2022. 2, 5

[35] Ashish Vaswani, Noam Shazeer, Niki Parmar, Jakob Uszkoreit, Llion Jones, Aidan N Gomez, Łukasz Kaiser, and Illia Polosukhin. Attention is all you need. *Advances in neural information processing systems*, 30, 2017. 3

[36] Liao Wang, Jiakai Zhang, Xinhang Liu, Fuqiang Zhao, Yanshun Zhang, Yingliang Zhang, Minye Wu, Jingyi Yu, and Lan Xu. Fourier plenoctrees for dynamic radiance field rendering in real-time. In *Proceedings of the IEEE/CVF Conference on Computer Vision and Pattern Recognition*, pages 13524–13534, 2022. 2

[37] Zhou Wang, Alan C Bovik, Hamid R Sheikh, and Eero P Simoncelli. Image quality assessment: from error visibility to structural similarity. *IEEE transactions on image processing*, 13(4):600–612, 2004. 7, 9

[38] Chung-Yi Weng, Brian Curless, Pratul P Srinivasan, Jonathan T Barron, and Ira Kemelmacher-Shlizerman. Humannerf: Free-viewpoint rendering of moving people from monocular video. In *Proceedings of the IEEE/CVF conference on computer vision and pattern Recognition*, pages 16210–16220, 2022. 2

[39] Qiangeng Xu, Zexiang Xu, Julien Philip, Sai Bi, Zhixin Shu, Kalyan Sunkavalli, and Ulrich Neumann. Point-nerf: Point-based neural radiance fields. In *Proceedings of the IEEE/CVF Conference on Computer Vision and Pattern Recognition*, pages 5438–5448, 2022. 2

[40] Ziyi Yang, Xinyu Gao, Wen Zhou, Shaohui Jiao, Yuqing Zhang, and Xiaogang Jin. Deformable 3d gaussians for high-fidelity monocular dynamic scene reconstruction. *arXiv preprint arXiv:2309.13101*, 2023. 3, 8

[41] Taoran Yi, Jiemin Fang, Xinggang Wang, and Wenyu Liu. Generalizable neural voxels for fast human radiance fields. *arXiv preprint arXiv:2303.15387*, 2023. 2

[42] Wang Yifan, Felice Serena, Shihao Wu, Cengiz Öztireli, and Olga Sorkine-Hornung. Differentiable surface splatting for point-based geometry processing. *ACM Transactions on Graphics (TOG)*, 38(6):1–14, 2019. 3, 4

[43] Alex Yu, Ruilong Li, Matthew Tancik, Hao Li, Ren Ng, and Angjoo Kanazawa. Plenoctrees for real-time rendering of neural radiance fields. In *Proceedings of the IEEE/CVF International Conference on Computer Vision*, pages 5752–5761, 2021. 2

[44] Lequan Yu, Xianzhi Li, Chi-Wing Fu, Daniel Cohen-Or, and Pheng-Ann Heng. Pu-net: Point cloud upsampling network. In *Proceedings of the IEEE conference on computer vision and pattern recognition*, pages 2790–2799, 2018. 2

[45] Kai Zhang, Gernot Riegler, Noah Snavely, and Vladlen Koltun. Nerf++: Analyzing and improving neural radiance fields. *arXiv preprint arXiv:2010.07492*, 2020. 2

[46] Richard Zhang, Phillip Isola, Alexei A Efros, Eli Shechtman, and Oliver Wang. The unreasonable effectiveness of deep features as a perceptual metric. In *Proceedings of the IEEE conference on computer vision and pattern recognition*, pages 586–595, 2018. 7, 9

[47] Matthias Zwicker, Hanspeter Pfister, Jeroen Van Baar, and Markus Gross. Surface splatting. In *Proceedings of the 28th annual conference on Computer graphics and interactive techniques*, pages 371–378, 2001. 3